Nonaxisymmetric Energy Deposition Pattern on ASDEX Upgrade Divertor Target Plates during Type-I Edge-Localized Modes

T. Eich, A. Herrmann, J. Neuhauser, and ASDEX Upgrade Team

Max-Planck-Institut für Plasmaphysik, EURATOM Association, Boltzmannstrasse 2, D-85748 Garching, Germany

(Received 5 June 2003; published 6 November 2003)

In the ASDEX Upgrade tokamak, complex power deposition structures on the divertor target plates during type-I edge-localized modes (ELMs) have been discovered by fast (few microseconds), two-dimensional (40×40 cm^2) infrared thermography. In addition to the usual axisymmetric power deposition line near the separatrix, there appear, statistically distributed, several laterally displaced and inclined stripes, mostly well separated from each other and from the main strike zone. These structures are interpreted as footprints of approximately field aligned, helical perturbations at the low field side of the main plasma edge related to the nonlinear ELM evolution. Based on this picture, the ELM related mode structure can be derived from the target load pattern, yielding on average toroidal mode numbers in a range of 8–24.

DOI: 10.1103/PhysRevLett.91.195003 PACS numbers: 52.55.Rk

Observation.—Operation in H mode [1] is generally assumed as the most likely scenario for next step tokamak fusion devices. H-mode plasmas develop a pronounced edge transport barrier and, hence, rather steep edge gradients, which can drive a variety of instabilities, especially quasiperiodic barrier relaxations, well known in the literature as edge-localized modes (ELMs), see, e.g., [2]. The best global plasma performance is usually obtained in the type-I ELM regime with its sudden release of typically a few percent of the total stored energy [3] on short time scales lasting about 300–800 μs. The high resulting heat fluxes, however, may cause intolerable heat load particularly onto the divertor target plates [4] in future experiments like ITER [5]. Therefore, a detailed understanding of the energy transport in the scrape off layer (SOL) and deposition onto the target structures is mandatory and is currently sought by all major tokamak research groups.

The preferred diagnostic for divertor target load measurements is infrared thermography. Analysis of the detailed type-I ELM structure with sufficient space and time resolution, however, is usually beyond the capability of existing hardware. Therefore, on ASDEX Upgrade, a new infrared thermography system, combining a high data acquisition speed, with camera shutter speeds down to 4 μs and with a fairly large survey area of 40 cm in toroidal as well as poloidal directions, was recently installed. It has a reasonable spatial resolution of 3.5×3.5 mm^2 per pixel on the target surface. This system has been applied to the easily accessible upper divertor with its flat and open target geometry, as illustrated in Fig. 1. The heat fluxes on the target surface are calculated by applying the standard numerical solution of two-dimensional heat diffusion equations [6] to the evolution of the target tiles' surface temperatures.

Furthermore, in order to increase the sensitivity of the measurements, carbon tiles with different surface properties, particularly in respect to their heat conductivities, are used. At the separatrix position, where the largest power load on the target plates is expected, newly installed target tiles with virgin surface and therefore the best possible heat conductivity are positioned (displayed as dark solid tiles of the upper divertor in Fig. 1 and toroidally extended tiles in the center of Fig. 2). In the area remote from the separatrix (displayed as light solid tiles of the upper divertor in Fig. 1) the surfaces of the installed target tiles have been exposed to the plasma over a period of 10 years of operation, causing changes of the plasma exposed surface properties [7]. Therefore, high transient temperature increases are measured, even when exposed to very low heat fluxes [8]. This experimental setup is well within the requirements for detailed estimation of the heat flux evolution, particularly during fast events like type-I ELMs in H-mode discharges.

Recent experiments have been run using the upper single null (USN) magnetic field geometry restricting the plasma-wall interaction nearly exclusively to the upper divertor target tiles, which lie in the visual field of the new IR camera system. With this setup, H-mode discharges exhibiting type-I ELMs display a multifaceted heat flux pattern upon the outer divertor target plates during the ELM power deposition phase. Figure 2 shows the temperature distribution on the target surface during a type-I ELM, as recorded by the infrared system (#16713, $I_p = 0.8$ MA, $B_t = -2.0$ T, $P_{\mathrm{NBI}} = 5$ MW).

In addition to the usual axisymmetric strike point line, about three to five narrow, nonaxisymmetric, and slightly inclined stripes are routinely observed in the remote region between 80 to 160 mm radially outwards from the strike point line.

Each of the nonaxisymmetric stripes has a width of about 10 mm, measured perpendicular to its toroidal extension. The distance between the stripes is also about 10 mm. The large variation in temperature in the toroidal direction occurs because of the gaps between the tiles in toroidal (and poloidal) directions.

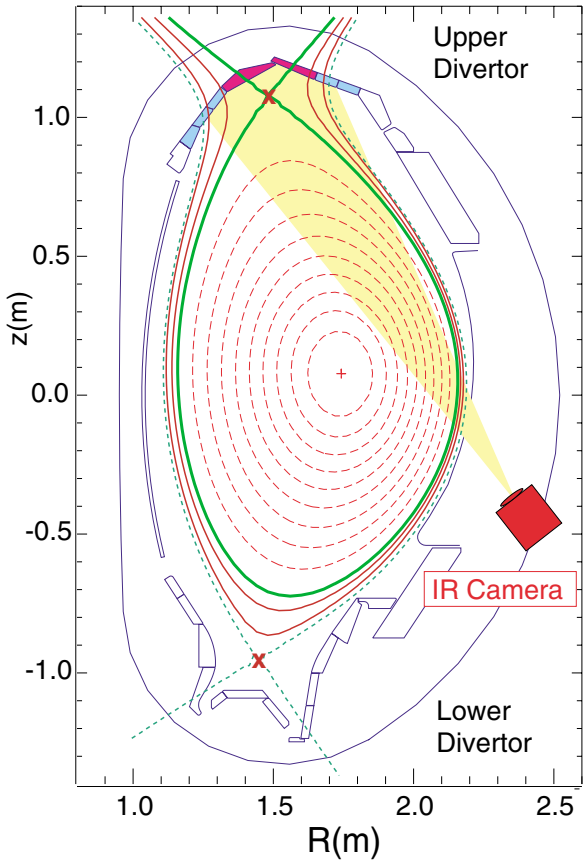

FIG. 1 (color online). Poloidal cross section of ASDEX Upgrade with upper single null magnetic equilibrium configuration + location of the infrared system (#16724). Solid line, first separatrix with upper x point; dashed line, second separatrix with lower x point.

The inclination angle of the stripes changes sign with toroidal magnetic field reversal, i.e., by reversing global field line helicity, as shown in Fig. 3 (#16718, $I_p = 0.8$ MA, $B_t = +2.0$ T, $P_{\mathrm{NBI}} = 5$ MW). Furthermore, the heat flux structure of various ELMs appears at varying radial positions on the target structure and is much more pronounced in discharges with a negative B-field direction and a $\vec{B} \times \nabla B$ drift pointing downwards from the upper x point towards the core region as compared to the discharges with positive B field and a $\vec{B} \times \nabla B$ drift pointing upwards. This behavior is routinely observed when ASDEX Upgrade is configured for USN geometry. Notice that the ratio between the inboard and outboard ELM power depositions changes with the B-field direction, such that more power is deposited on the outboard target tiles when the $\vec{B} \times \nabla B$ direction is pointing downwards, away from the upper x point. Every observed type-I ELM has shown these stripes, without exception. Until now, no evidence for a corresponding structure has been identified on the inboard target plates.

The evolution of the power deposition profiles can be closely studied by reducing the frame size for the infrared camera. This yields a higher frame frequency equal to

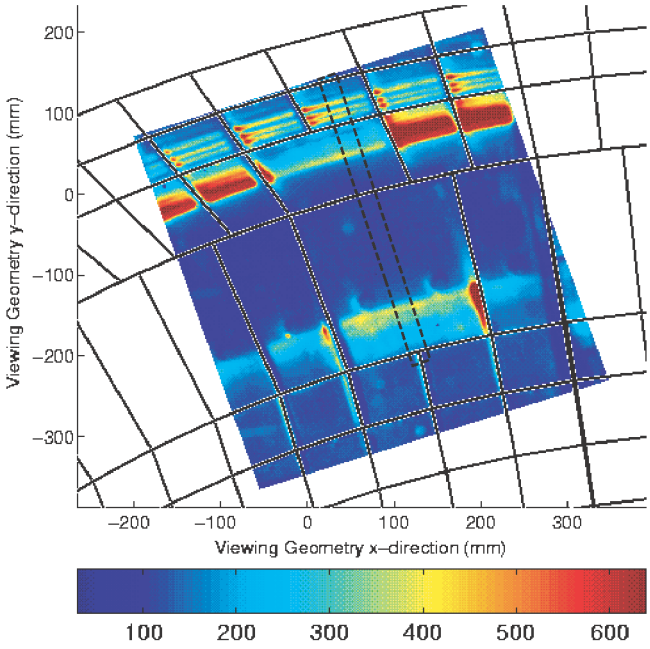

FIG. 2 (color online). The target surface temperature pattern (in degrees Celsius) during this type-I ELM event shows the characteristic nonaxisymmetric structures in the remote area of the strike line (#16713).

136 μs, with a shutter speed of 20 μs. The size of such a frame is shown in Fig. 2 as the dashed black box in the middle of the picture. From the evolution of the temperature profiles, the heat flux evolution over the same time is calculated.

Figure 4 shows the evolution of heat flux profiles (#16724, $I_p = 0.8$ MA, $B_t = -2.0$ T, $P_{\mathrm{NBI}} = 5$ MW), calculated from the temperature profiles of a type-I ELM event. Different details of the ELM power profile evolution should be noted. Notice that, for $\Delta t = 136$ μs, the heat flux has a single peak (corresponding to one stripe) on the outer target surface (shaded band region

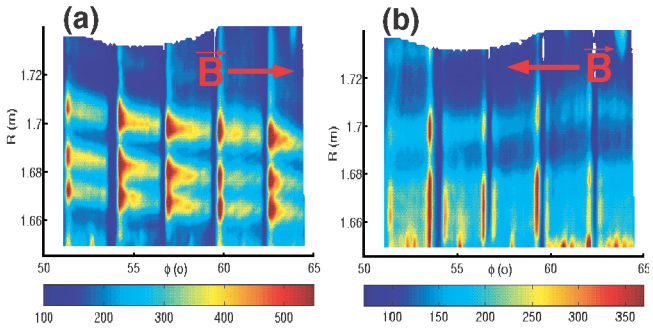

FIG. 3 (color online). The inclination of heat fluxes within type-I ELMs changes its orientation with the B-field direction. (a) was taken with a negative B-field direction ($\vec{B} \times \nabla B$ pointing away from the upper x point). In (b) the B field has been reversed ($\vec{B} \times \nabla B$ pointing towards the upper x point). The heat flux on the outer target structure is more pronounced in discharges with negative B-field direction as compared to the discharges with positive B field [(a) #16713; (b) #16718].

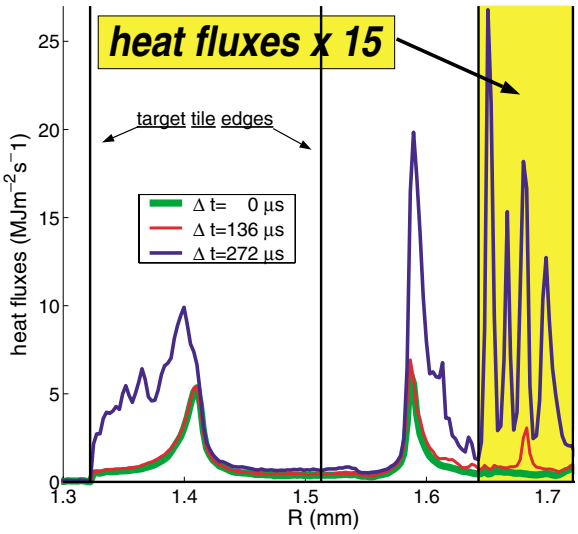

FIG. 4 (color online). The evolution of the structure's target profiles with a time resolution of 136 μs and shutter speed of 20 μs. The peaks at $\Delta t = 0$ μs correspond to the power load on the strike line before the ELMs appear. The following two profiles ($\Delta t = 136$ μs and $\Delta t = 272$ μs) show the temporal evolution during a type-I ELM (#16724). For the latter two profiles the heat fluxes in the shaded band region are oversized by a factor of 15.

in Fig. 4). Simultaneously, a very small increase of the power deposited to the outer strike line can be observed. No increase of heat flux can be observed during this phase on the inner strike line. In the next heat flux profile ($\Delta t = 272$ μs) the structure is much more developed, with at least four peaks visible on the outside target.

After analysis of the data (up to 1000 ELMs are recorded in a single discharge of which 200 are analyzed), the following picture emerges of the heat flux dynamics. The heat fluxes in the various structures appear at different times; these times (tens of microseconds) are smaller than a time gap between two consecutive recorded heat flux profiles. The lifetime of a single stripe appears to be less than that of the overall ensemble of stripes, which continues as long as power is deposited towards the strike line. This means that the power deposition and most likely the power release from the pedestal as well happens in a burstlike temporal sequence. A little less than 3% of all the deposited energy is calculated to appear in the profile on the remote tile surface (shaded band region in Fig. 4).

Interpretation.—This target pattern may be qualitatively understood in terms of the edge field line topology of poloidal divertor equilibria. Let us consider a narrow helical flux bundle in the main chamber low field side SOL, loaded by plasma expelled from the pedestal region during the nonlinear phase of an unstable high-(n, m) mode as expected during ELMs [9]. Our choice of field line starts at the low field side is based on the experience that the ELM energy loss comes predominantly from this bad curvature side. This is shown in ASDEX Upgrade double null discharges following the experimental method which was demonstrated by DIII-D [10] and MAST [11].

When this flux bundle is mapped along field lines to the upper outer divertor target, it is distorted by the strong shear close to the upper x point approaching asymptotically the separatrix strike line [12]. The key mechanism behind is that the closer a field line passes by the x point, the higher the connection lengths gets and the more it is displaced in the toroidal direction, when arriving at the target. This leads to a characteristic relation between the radial distance and the toroidal angle of the intersecting point of the helical flux bundle on the target plates, namely, a spiral (Fig. 5, top panel). The intersection structure on the inner target plates is more complex, since, on the way around the plasma bottom, field lines between the first and the second separatrix (see Fig. 1) are influenced first by the lower and then by the upper x points, resulting in a combined double spiral structure with both separatrices as asymptotes (Fig. 5, bottom panel). Field lines outside the second separatrix are not connected to the upper divertor.

Assuming that, to lowest order, energy is transported strictly along field lines, and identifying the inclined stripes, seen by thermography, with the spiral arms in Fig. 5, this simple picture reproduces all the essential

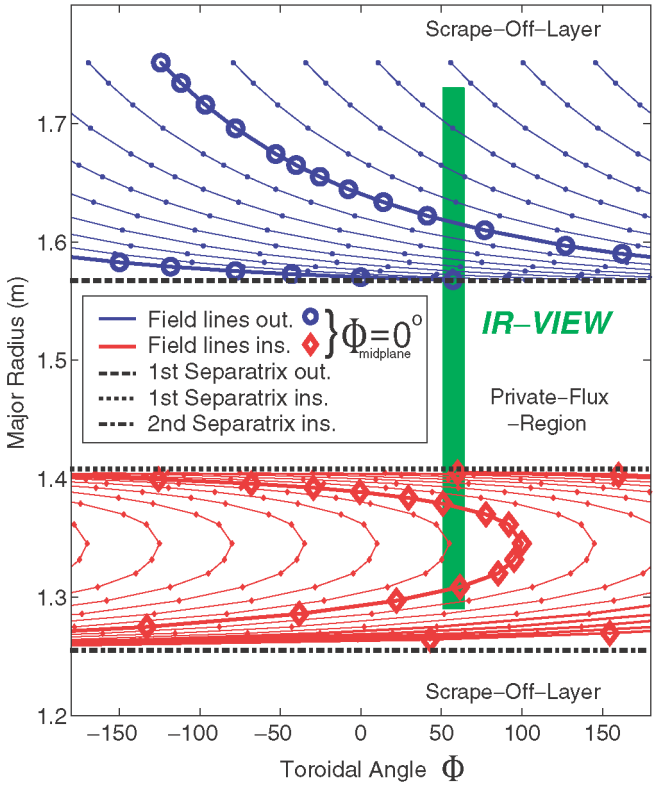

FIG. 5 (color online). Field lines, originating from the outer midplane SOL along eight toroidally equally separated major radius lines, intersect the divertor target plates in a characteristic pattern (see text). The rectangular area displays the experimental observation area by the infrared system (#16713).

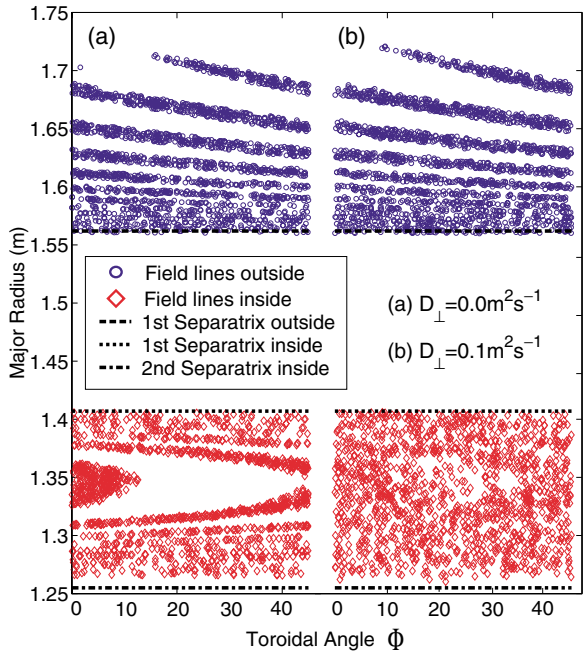

FIG. 6 (color online). The pattern of field lines intersecting the divertor target plates, including transport processes like field line ergodization [(a),(b)] and particle diffusion [only (b)]. The clearest part of the pattern is at the periphery of the outer strike zone, in agreement with the experimental observation.

features seen on the outer target, and we may try to reconstruct the underlying mode structure in the main chamber edge from it, at least in a statistical sense. As we see several displaced stripes appear simultaneously, we identify them as several toroidally displaced origins of energy release in the midplane. From these we may define an effective toroidal mode number n, given by 2π divided by the toroidal displacement between two neighboring origins in the midplane. Typically, n values in the range 8–24 have been found this way in the examined plasmas, when the time of the maximum power deposition on the target has been taken. One should notice that the more or less statistical distribution of the stripes in toroidal position means that we obviously see at best weakly correlated helical structures rather than coherent modes, as expected for a burst of highly nonlinear instabilities. On the other hand, the fact that, nevertheless, individual spirals during a specific ELM appear with a jitter of only a few tens of microseconds relative to each other indicates that there is still enough interaction, e.g., on a toroidal shear Alfvén wave time scale, for a fast trigger cascade, once a fast instability starts to grow locally.

Presently, no comprehensive, nonlinear ELM model is available for more detailed comparison. To get, nevertheless, a feeling of the influence of cross field transport and magnetic perturbations on the target pattern, we have constructed an extended field line tracing model representing these effects at least in a paradigmatic form. In essence, we superpose an external magnetic field perturbation onto the axisymmetric plasma equilibrium (ignoring any skin effect) by adding N magnetic dipoles, again at the low field side midplane only, equally distributed toroidally for simplicity and about 15 cm away from the separatrix. From the resultant wide n, m spectrum (with $n \geq N$) the magnetic configuration responds primarily to resonant modes with $m/n \approx q$ to produce ergodization inside a helically perturbed surface, and an essentially laminar SOL region outside [13]. The resultant configuration should crudely resemble the one during the nonlinear ELM evolution, where similar edge perturbation fields are produced by dissipative electromagnetic plasma instabilities and the related internal edge currents. Effective radial transport of particles from the pedestal into SOL and convective flow to target plates is then simulated by following a large number of field lines, including random cross field steps to represent some microscopic cross field diffusion, until they hit the targets (or leave the computational domain).

The result is shown in Fig. 6 for $N = 8$ (a) without and (b) with an artificial diffusion coefficient $D = 0.1\ \mathrm{m^2\,s^{-1}}$, if related to deuterons with 1 keV parallel energy. For (a) the spiral structures on both target plates are fully consistent with those of the simple equilibrium mapping in Fig. 5. For $D = 0.1\ \mathrm{m^2\,s^{-1}}$, however, the inboard structure is washed out, while the outer target spirals survive (calculations with even higher D values have been run with the same result). This diffusion dependence might explain the absence of pronounced structures at the inner target. Altogether, this crude ELM mock-up model seems to support our geometrical interpretation of the observed pattern.

[1] F. Wagner *et al.*, Phys. Rev. Lett. **49**, 1408 (1982).
[2] H. Zohm, Plasma Phys. Controlled Fusion **38**, 105 (1996).
[3] A. Loarte *et al.*, Plasma Phys. Controlled Fusion **44**, 1815 (2002).
[4] T Eich *et al.*, J. Nucl. Mater. **313–316**, 919 (2003).
[5] ITER Physics Expert Group, Nucl. Fusion **39**, 2391 (1999).
[6] A. Herrmann *et al.*, Plasma Phys. Controlled Fusion **37**, 17 (1995).
[7] P. Andrew *et al.*, J. Nucl. Mater. **313–316**, 135 (2003).
[8] A. Herrmann *et al.*, Europhys. Conf. Abstr. **25**, 2109 (2001).
[9] J. Connor, Plasma Phys. Controlled Fusion **40**, 191 (1998).
[10] C. Lasnier *et al.*, J. Nucl. Mater. **290–293**, 1093 (2001).
[11] A. Kirk *et al.*, J. Nucl. Mater. **313–316**, 1081 (2003).
[12] A. Punjabi *et al.*, Phys. Rev. Lett. **69**, 3322 (1992).
[13] J. Neuhauser, Plasma Phys. Controlled Fusion **31**, 1551 (1989).